Fundamental research on the voltammetry of polycrystalline gold

Yang, S.


Geocentrism
Heliocentrism
关键，
不在于他们在哪，
而在于他们如何存在。
The key is,
not where they are,
but how they exist.

3

Evolution of amorphous metal oxide structures during catalysis

Abstract

Amorphous metal oxide surfaces play a key role in electrocatalysis. Yet at present we know very little about the atomic structure of these amorphous metal oxide surfaces and the precise phenomena occurring at the liquid solid interface of these materials. Here we show that under oxidative conditions Au^{3+} cations are constantly being formed within amorphous gold oxide, and that these are the main cause for previously not understood phenomena such as non-Nernstian potential shifts. The Au^{3+} cations play a crucial role in the chemistry of gold oxide, where these form bonds with nucleophiles present within the amorphous gold oxide layer and the electrolyte solution, thereby dominating the interactions at the solid-liquid interface. Moreover we show that these exposed cationic sites play a crucial role not only in the structure of the solid-liquid interface but also actively take part in the catalytic water oxidation reaction.

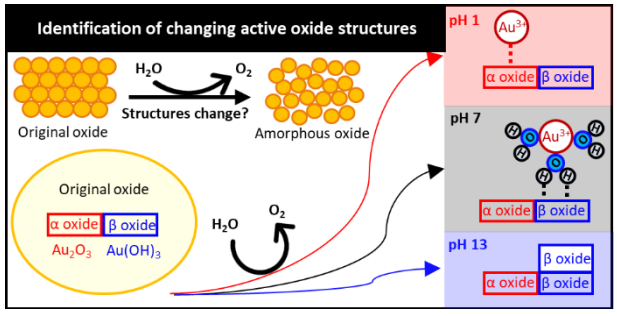

Keywords: Oxygen Evolution Reaction, Amorphous Gold Oxide, Non-Nernstian Shifts, Solid-Liquid Interface Structure, Gold Cation Interactions

3.1 Introduction

Metal oxide catalysts display a remarkable activity for a wide plethora of chemical reactions.[1-4] Despite the large interest in these catalytic materials by the scientific community, it remains a major challenge to accurately describe the real surface structure of metal oxides under realistic catalytic conditions. At present, our understanding of the metal oxide structure on the atomic–scale mainly relies on ex situ spectroscopy techniques in vacuum,[5-7] and computations on well-defined and highly symmetric metal surfaces. However, the corrosion and reconstruction of the metal oxide surface during catalysis results in the formation of amorphous structures, that are largely different than the original well–defined crystalline materials studied in vacuum and by computations.[7-10] Until now, the fundamental origins of the self–reconstruction processes occurring at these oxides during catalysis are not understood, and the active sites in these amorphous catalysts have rarely been discussed. These limitations are not only due to the lack of suitable in situ techniques to capture the complete phase transformation, but also due to a lack of a sound electrochemical theory that describes the phenomena occurring at the liquid–solid interface precisely.[7, 11] One of these ill-understood phenomena is the relationship between the peak potentials and pH under realistic conditions.

The potential where an electrochemical reaction ($Oxidant + ne^- \rightleftharpoons Reductant$) may occur can be described by the Nernst equation. This equation is written as $E = E^0 - \frac{RT}{nF} ln \frac{[reductant]}{[oxidant]}$, and defines a quantitative relationship between the measured potential (E) and the standard potential (E^0) as a function of the activities of all participating chemical species. The Nernst equation dictates that the reduction potential of a metal oxide ($M_2O_x + 2xH^+ + 2xe^- \rightarrow 2M + xH_2O$) should not change as a function of pH, with respect to the potential of the reversible hydrogen electrode ($RHE: 2H^+ + 2e^- \rightleftharpoons H_2$). The potential difference between the redox reaction and the RHE electrode should remain the same (it should follow Nernstian behavior) as both these redox reactions have the same 1:1 ratio of electrons and protons involved. However, anomalous potential shifts, i.e. “non–Nernstian behavior” are often encountered in many oxide reduction processes. Moreover, these anomalous shifts are extensively observed in many relevant electrochemical reactions such as the evolution and

reduction of oxygen,[12-14] the evolution, the oxidation of hydrogen,[15, 16] the oxidation of methanol, [17, 18] and the CO_2 reduction reaction.[19, 20] Thus far the non–Nernstian behavior of both metal oxide reduction and the aforementioned electrocatalytic reactions is rarely systematically studied. Moreover, many explanations for Non-Nernstian behavior of oxide reduction given in the past are vague (see the supplementary materials, section S1 for a brief literature overview) [11, 21]. In studies concerning catalytic reactions at metal oxide layers, it has often been assumed that the surface structure of the catalyst remains unchanged during the catalytic reaction. It is well known that this is not the case[2, 7].

In this manuscript we show that the non-Nernstian behavior of gold oxide reduction peak is intimately linked to the precise and ill-understood events that occur at the oxide surface. Gold is the noblest metal and – as so often demonstrated for new fundamental breakthroughs such as the exploration of metals' inert properties[22] and investigations into the structures of electrified interfacial water[23, 24] – the most appropriate metal for the oxide reduction studies targeted in this manuscript. It has been firmly established that the +III oxidation state is the only relevant oxidation state in gold oxide chemistry [25, 26] and the chemisorption of electrolytes on gold is weak.[27] The effect of oxidation state changes and electrolyte co–adsorption on non-Nernstian shifts therefore can be largely excluded. Employing gold electrodes, we show that non-Nernstian shifts are actually caused by the reduction of charge imbalanced Au^{3+} species. It is these Au^{3+} species that are dominating the interactions between the metal oxide surface and the electrolyte at the solid-liquid interface. In addition, these Au^{3+} species play a critical role in the oxygen evolution reaction. In general, our findings shed significant light on the atom–atom interactions taking place at the solid–liquid interface, and the reconstruction processes taking place at gold oxides during the oxygen evolution reaction.

3.2 Experimental results

The initial stages of the formation of gold oxidation during an oxidation reaction are associated with the sequential formation of sub–lattices of O and OH.[11] The O and OH chemisorb on gold to form stable Au_2O_3 (α–type) and $Au(OH)_3$ (β–type) monolayers, respectively. The existence of Au–O bonds in case of α oxide and Au–OH bonds in case of β oxide have been established previously by in situ Surface–Enhanced Raman Spectroscopy

(SERS).[8] At early stages of oxide formation, the reduction peak potentials of the formed α (E_α) and β (E_β) oxides follow the Nernst equation (fig. S1). In other words, E_α (1.23 V) and E_β (1.1 V) (see Fig. 1A) are independent of the pH providing that upper limit of the CV (E_+) is kept at an oxidation potential below 1.45 V vs RHE. However, non–Nernstian shifts can be observed when E_+ is systematically varied at higher potentials (Fig. 1A). When E_+ is set to a higher potential, E_α shifts negatively with higher E_+ in both acidic and neutral conditions (pH ≤ 10). In addition, E_α is pH dependent so that the E_α vs pH plot shows an increasing slope versus the RHE scale (Fig. 1B). A different behavior was observed in case of E_β (Fig. 1C). When E_+ is set below the onset potential of the oxygen evolution reaction (E_{OER}), E_β initially shifts negatively with increasing E_+ in the pH range of 4–10. The closer the pH of the solution is to 7, the larger the shift is that can be observed. However, these large negative shifts of E_β do not occur when E_+ is set above E_{OER}. (fig. S6) Interestingly, in alkaline solutions, E_β shows no potential shifts if E_+ is chosen below E_{OER} but moves gradually negative when E_+ is set above E_{OER} (Fig. 2C). These oxides reduction peaks show non–Nernstian behavior consistently and show only small deviations with the scan rate (0.01 to 0.5 V/s) (fig. S2). This indicates that the non–Nernstian behavior is not caused by kinetic effects, and cannot be explained by local pH effects (see fig. S2). Moreover, these non–Nernstian shifts of the α and β peaks do not depend on the cation (Li^+, Na^+, K^+, Cs^+) (see fig. S3) or the anion (SO_4^{2-} and ClO_4^-)[8] present in the electrolyte. We therefore can also exclude electrolyte adsorption playing a role.

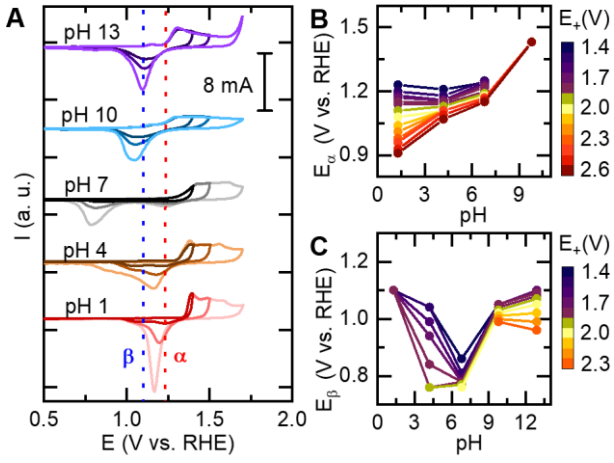

Fig. 1 The reduction of gold oxide follows non–Nernstian behavior. (**A**) CVs of gold in electrolyte solutions of different pH at 50 mV/s. 1.23 V (Red dash lines) and 1.1 V (Blue dash lines) represent the reduction peak potentials of α and β oxide at their initial formation stages, respectively (see fig. S1). (**B**) The potential of the α peak plotted as a function of pH and E_+. (**C**) The potential of the β peak plotted as a function of pH and E_+. Potentials are plotted versus RHE, i.e. a horizontal line would represent a Nernstian shift in B and C.

The release of gold cations during the oxide reduction process in acidic solutions has been reported previously in rotating ring–disk electrode (RRDE) experiment [28] and inductively coupled plasma mass spectrometry (ICP–MS) in a scanning flow cells (SFC).[29] As the +III oxidation state is the only relevant oxidation state in gold oxide chemistry (*22, 23*), we assume Au^{3+} is detected, but that we cannot fully rule out larger aggregates. Motivated by these observations, we investigated whether the existence of Au^{3+} ions which charge is not balanced due to a lack of neighboring oxide atoms cause the non–Nernstian shifts observed in these RRDE experiments (Fig. 2A). In an acidic solution, no Au^{3+} could be detected in the reverse scan in the E_+ range of 1.3 to 1.45 V, even though both α and β oxide are already formed at these potentials (Fig. 2B). When E_+ is set above 1.5 V, more and more Au^{3+} can be detected on the ring simultaneously with reduction of α oxide at the disk. Under conditions where Au^{3+} could be detected, the α peak shows a non–Nernstian shift (Fig. 2B). In an alkaline solution, the release of Au^{3+} also can be observed in case of β oxide, providing that E_+ is set at a higher potential than 1.9 V. Also these latter conditions trigger a negative non–Nernstian shift of the β peak (Fig. 2C). The α peak in acidic media and the β peak in alkaline solutions follow the same trend: If there is a non–Nernstian potential shift, this is always accompanied by the detection of gold cations on the RRDE ring.

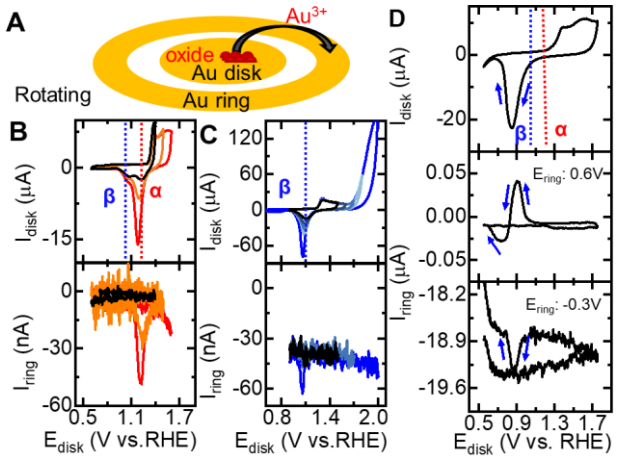

Fig.2 Au^{3+} release during gold oxide reduction. (**A**) Schematic of a rotating ring–disk electrode (RRDE) used to detect Au^{3+} that is released from the gold oxide disk and detected at the ring. (**B–D**) RRDE measurements of gold at 50 mV/s and 1600 rpm. The red and blue dashed lines represent the reduction peak potential of initial formation stage of α and β oxide, respectively. (**B**) The electrolyte is 0.1 M $HClO_4$, and E_{ring} is set at 0.6 V. (**C**) The electrolyte is 0.1 M NaOH, and E_{ring} is set at 0.9 V. (**D**) The electrolyte is 0.1 M $NaClO_4$, and E_{ring} was set at 0.6 V (middle) and –0.3 V (bottom), respectively. Different colors represent various CVs at different upper limit potentials.

When the potential of the gold ring (E_{ring}) is kept at 0.6 V in a neutral solution, initially an unusual positive current was observed on the ring, while the negative current signal that can be expected for Au^{3+} reduction was observed on the ring only after most of the β oxide is reduced at the disk (see middle part of Fig. 2D). When we match the lower potential limit ($E_–$) of the CV experiment with $E_β$, the negative current on the ring will emerge in the following positive scan (fig. S4A–D). This points to a delayed reduction response that is preceded by unknown oxidation process. Interestingly, the typical negative current of Au^{3+} reduction without the presence of any positive current can be observed immediately when E_{ring} is set below 0 V (see lower part of Fig. 2D).

All these observations illustrate that the observed non–Nernstian behavior is accompanied by the presence of Au^{3+} in solutions of all pH, and independent of whether α or β oxide is involved.

The mass change of the gold surface was investigated during CV experiments by characterizing the frequency response using a electrochemical quartz crystal microbalance (EQCM), whose oscillation frequency is inversely proportional to the change of mass on its surface (Fig. 3A).[30] These mass changes of the oxide reduction reaction do not only include the removal of lattice oxygen atoms, but also involve effects of the rigid double layer when bound water and electrolyte is dissociated.[31-33] While the mass changes very well fit to the amount of lattice oxygen atoms present in the oxide under conditions where no Au^{3+} is present, these mass changes become significantly larger in experiments with high E_+ where a lot of Au^{3+} is formed (fig. S8). This means that significantly more water and electrolyte molecules are bound when Au^{3+} is present at the electrode interface, and that one can use EQCM as a diagnostic tool to monitor Au^{3+} removal from the electrolyte surface. An onset potential of mass loss (E_ψ) appears during the oxide reduction process and can be correlated to E_α and E_β in solutions of different pH, shown in Fig 3B–D. When the two oxides show no non–Nernstian behavior in an acidic solution (E_+<1.5 V), the mass loss was observed only after the two oxides have been completely reduced (Fig. 3B). Once E_+ is set above 1.5 V, E_ψ immediately changes to the same potential as E_α and shifts negatively with E_α when E_+ is increased further. However, the shift of E_ψ will stop when E_+ >2.1 V while the shift of E_α continues so that the two potentials gradually separate for E_+ set in the range of 2.1 to 2.6 V. The separation between E_α and E_ψ also appears in the same range (2.1 to 2.6 V) in neutral solutions (Fig. 3C). When E_+ is lower than 1.9 V at neutral conditions, E_ψ only appears in the first half of the β peak but shows no relationship with the α peak even though a shift of the α peak can be observed. The correlation between E_ψ and E_β gradually turns into a correlation between E_ψ and E_α in a potential region from 1.9 V to 2.1 V (see fig. S6). In an alkaline solution (Fig. 3D), the correlation between E_ψ and E_β is more consistent. When E_+ is set below 1.7 V, E_ψ and E_β were found at 1.13V, and 1.10 V, respectively. When E_+ is set above 2 V, E_β and E_ψ will shift simultaneously with a constant potential difference of $E_\psi - E_\beta = 0.04$ V. Overall, the E_ψ shift shows a direct relationships with the non–Nernstian behavior of the α and/or β peaks, which have been correlated to the release of Au^{3+} by our RRDE experiments.

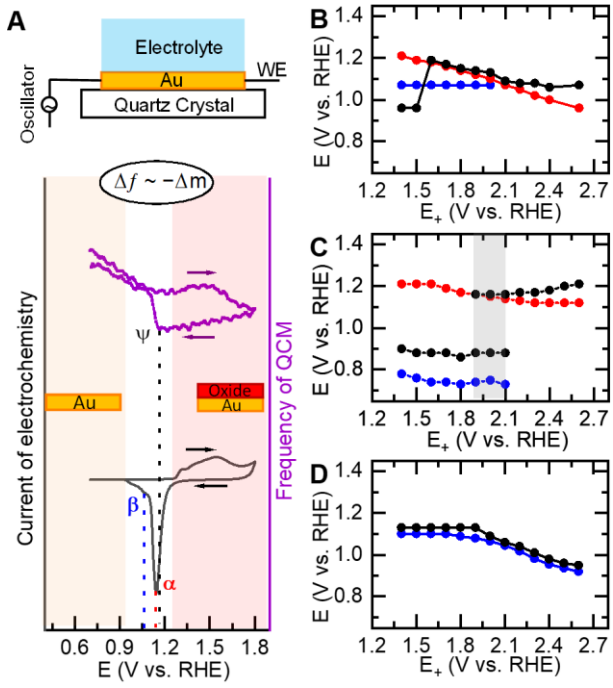

Fig. 3 The onset potential of surface mass loss during the gold oxides reduction process. (**A**) Schematic of the electrochemical quartz crystal microbalance (EQCM) used to detect the surface mass change. Show are the current (in black) and the frequency change (in purple) as function of the applied potential during an EQCM CV experiment. (**B–D**) E_α (red line), E_β (blue line) and the onset potential of mass loss (E_ψ, black line) as a function of E_+ in 0.1 M $HClO_4$ (**B**), $NaClO_4$ (**C**) and NaOH (**D**) (More details are shown in fig. S5–7).

3.3 The relationship between non–Nernstian behavior and the surface structure

Gold exhibits a strong covalent bonding character due to a relatively small 6s–5d energy gap and therefore enhanced s–d hybridization.[34] Two initial stable covalent oxides are formed by chemisorption of O and OH on gold, i.e. Au_2O_3 (α oxide) and $Au(OH)_3$ (β oxide).The Nernst equations of both α oxide ($Au_2O_3 + 6H^+ + 6e^- \rightarrow 2Au + 3H_2O$) and β oxide ($Au(OH)_3 + 3H^+ + 3e^- \rightarrow Au + 3H_2O$) dictate that the corresponding reduction potentials should not change with the pH of the solution on the RHE scale, illustrated in fig. S9. It is essential that the reaction stoichiometry is correct when the equilibrium potential of a redox half–reaction is calculated by applying the Nernst equation. At high electric fields, insulating gold oxide growth occurs via the "Mott–Cabrera" mechanism, where formed gold cations

($Au \leftrightharpoons Au^{3+} + 3e^-$) are injected into the oxide and migrate from the oxide layer into oxide–solution interface.[35] The electronic structure of such initial covalent oxides is expected to change dramatically when the amount of ionic gold ions increases within these oxide layers.

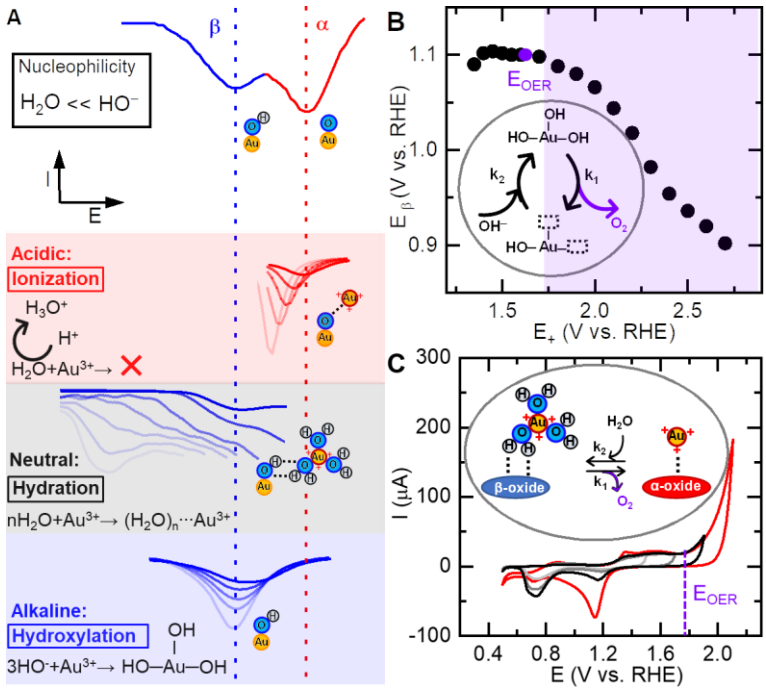

Fig.4 Ionization, Hydration and Hydroxylation of gold cation within gold as a function of pH. (A) Non–Nernstian responses for ionic bonding of Au^{3+} on α oxide (light red region); Non–Nernstian responses for hydrogen bonding of hydrous Au^{3+} on β oxide (light grey region); and Nernstian responses for covalent bonds of hydroxylated Au^{3+} on β oxide (light blue region). The red and blue dashed lines represent the reduction potential of initial formed thin α oxide (Au_2O_3) and β oxide ($Au(OH)_3$), respectively. The red and blue line represent the α and β reduction peak in CVs, respectively and their color changes (from dark to light) reflect the peak change with the increase of E_+ in different pH solutions. (**B**) The change of E_β at pH 13 when E_+ is set below and above E_{OER}. (**Insert B**) Proposed mechanism of mutual transformation of ionized Au^{3+} and hydroxylated Au^{3+} within $Au(OH)_3$ in the OER process in an alkaline solution. (**C**) The change of CVs in pH 7 when E_+ is set below and above E_{OER}. (**Insert C**) Proposed mechanism of mutual transformation between ionized Au^{3+} and hydrous Au^{3+} within α and β oxide in the OER process in a neutral solution.

Now the formation of Au^{3+} ions has been firmly established, one can discuss the potential effects of its presence on the chemistry at the gold oxide – liquid interface. The characteristic of Au^{3+} is a lack of electrons, and consequently its structure will strongly depend on the availability of good nucleophiles present in solution. As observed, the variations in metal cations and anions present in electrolytes have minimal impact on the gold oxide reduction process (Fig. S3). This suggests that highly hydrated metal cations and anions exhibit relatively uniform behavior at the gold oxide-liquid interface. Therefore, the two main types of nucleophiles present in an aqueous solution are H_2O in acidic and neutral solutions, and OH^- in an alkaline solution. Their nucleophilicity is strongly pH dependent with $H_2O << HO^-$. Since the nucleophilicity of H_2O in strong acidic solutions is very poor as the existence of hydronium anions, Au^{3+} will predominantly adsorb on the exposed oxygen sites of Au_2O_3. These oxygen sites can act as Lewis base sites to form ionic bonds with Au^{3+}. These ionic bonds of $Au_2O_3 \cdots Au^{3+}$(ionized Au^{3+}) would then stabilize α oxide resulting in the negative shift of the α peak. The formation of these ionic bonds takes time, and if the scan rate is fast enough (50 mV/s to 10 V/s), the non–Nernstian behavior of the α peak will disappear and instead a reversible free Au^{3+} reduction peak appears at 1.31 V vs RHE, illustrated in (fig. S10). The reversible reduction of free Au^{3+} has been reported previously at high temperature (365 K) and at high $HClO_4$ concentrations .[36] The ionic bonds of ionized Au^{3+} rely on the balance of electrostatic forces between the Au^{3+} ions and oxygen sites. Consequently, every oxide reduction step results in cleavage of these ionic bonds, which explains why the onset of Au^{3+} release from α oxide is coincidental with the onset of the reduction of α oxide observed in our RRDE experiment (fig. S11A).

When the pH of the electrolyte solution increases to neutral conditions, the nucleophilicity of water increases. Therefore, Au^{3+} is expected to form interaction with water molecules, rather than the exposed oxygen sites of Au_2O_3, and will form hydration shells (hydrous Au^{3+}). Such a hydration shell can also easily stabilize β oxide–$Au(OH)_3$ through hydrogen bonding interactions that cause an obvious potential shift of the β peak. The competition between ionized Au^{3+} and hydrous Au^{3+} can be monitored by the change of the two reduction peaks (α and β) in a pH range between 4 and 7 (fig. S12). The non–Nernstian behavior of the α and β oxide

reduction peaks will disappear when the rotation rate of the RDE experiments is set at 3000 rpm. This is in agreement with an efficient removal of Au^{3+} upon rotation, as it is merely attached via weak non covalent interactions (fig. S13A–B).

Formation of Au^{3+} bound to the electrode surface via ionic or hydration shell interactions can be observed by Non–Nernstian shifts of E_α and E_β and can be traced by the EQCM signal E_ψ (Fig. 3). (see the supplementary materials, section S3) There the presence of E_ψ does not directly relate to removal of a particular metal oxide, but rather to the presence of Au^{3+} on the oxide surface, both in case of α and β oxide. It is important to note that the EQCM can only detect mass changes at the surface and is not affected by the reduction of free Au^{3+} ions in solution. Therefore, the separation of E_α and E_ψ can be used to estimate to what extend Au^{3+} is bound to the electrode surface, or whether the gold ion has become fully solvated (see the supplementary materials, section S4). When E_+ is set above 2.1 V, E_α and E_ψ separate. This indicates that binding of Au^{3+} to the surface has become saturated and more free Au^{3+} unable to bind to the Au_2O_3 surface has escaped from the rigid interface into the diffusion layer. More specifically, taking into account the precise moment when E_ψ and E_α deviate, the amount of Au^{3+} within α oxide can be quantitatively evaluated on basis of the slope of the α oxide reduction peak in E–pH diagrams. (see the supplementary materials, section S5) With the increase of E_+, the α oxide is changing from a covalent oxide (Au_2O_3) to a covalent–ionic oxide ($Au_2O_3 \cdots xAu^{3+}$), where x represents the amount of Au^{3+} forming ionic bonds per α oxide site. Based on the increasing slope of the E–vs–pH plots (Fig. 1B), x increases from 0 to 0.4 before OER starts and quickly reaches saturation (x~0.9) at 2.1 V during the OER process (table S1). In other words, we have now largely turned the Non–Nernstian behavior of the oxide reduction reaction into a Nernstian one by including the correct amount of Au^{3+} in the reaction stoichiometry.

When the pH of the solution is further increased to alkaline conditions, the main nucleophile present in solution is OH^- rather than H_2O. OH^- can form more stable covalent bonds with Au^{3+} (hydroxylated Au^{3+}). The bonding interaction between Au^{3+} and OH^- will produce new β oxide layers on top of the initially formed β oxide. The hydroxylation process

thereby ensures the uniformity and electrical neutrality of the β oxide, which therefore shows Nernstian behavior as E_β does not shift with pH.

3.4 The relationship between non–Nernstian behavior and reconstruction of the metal oxide during the OER

Although ionized Au^{3+}, hydrous Au^{3+} and hydroxylated Au^{3+} are the preferred structures in acidic, neutral and alkaline solution, respectively, as shown in Fig. 4A. These surface structures inevitably turn to ionic Au^{3+} at high rates of the oxygen evolution reaction (Fig. S5-7). It was previously reported the O_2 is produced from lattice-oxygen atoms [37] and that the oxygen evolution on $Au(OH)_3$ follows a Proton–Decoupled Electron Transfer process at alkaline conditions.[8] Fig. 4B shows the two main steps needed to form O_2 in an alkaline solution: (1) Formation of O_2 by lattice exchange between Au–OH covalent bonds leaving exposed sites on Au; (2) regeneration of $Au(OH)_3$ by coordination of hydroxide to the exposed sites on Au. The overall process must involve a delicate balance between these two reaction steps with the independent reaction rate constants k_1 and k_2. At low oxidation potentials, where $k_1 < k_2$, $Au(OH)_3$ retains its uniformity and electrical neutrality. Under these conditions, Au^{3+} release from $Au(OH)_3$ is not observed. Further increasing E_+ must result in $k_1 > k_2$. Under these conditions, Au^{3+} release from $Au(OH)_3$ becomes apparent. This ionization process likely takes place only on the outer layer of $Au(OH)_3$. This is in line with the RRDE experiments in alkaline solutions, where Au^{3+} release is observed only when the scanning potential approaches E_β where the outer layer of $Au(OH)_3$ is reduced (fig. S11B). A similar delicate balance exists between hydrous Au^{3+} and ionized Au^{3+} in neutral conditions (Fig. 4C). When $k_1 < k_2$, stable hydration shells of Au^{3+} are present within the β oxide even if E_+ is set slightly above E_{OER}. At higher oxidation potentials, where $k_1 > k_2$ and the free sites generated by elimination of O_2 are only sparsely replenished, ionized Au^{3+} on α oxide becomes the dominant surface structure. Since these non–covalent bonds are relatively weak, the mutual transformation between ionized Au^{3+} and hydrous Au^{3+} can be effected by rotation rates and rinsing of the electrode (see the supplementary materials, section S6).

3.5 Conclusions

We have confirmed that the non–Nernstian behavior of the electrochemical reactions and the precise reaction steps occurring on the electrode surface are intimately linked. More specifically, the non–Nernstian behavior of the gold oxide reduction reaction is due to charge imbalanced Au^{3+} present in the gold oxide layers that is being reduced in a reaction wherein no protons are involved. These Au^{3+} ions play a pivotal role in the surface chemistry of gold oxide and the chemical processes occurring that the solid-liquid interface. At the solid–liquid interface Au^{3+} is stabilized by ionic interactions with the gold oxide surface at acid conditions, via hydration shells under neutral conditions and upon hydroxide binding at alkaline conditions. Equilibria between these binding modes of Au^{3+} play a critical role in the OER mechanism wherein Au^{3+} is continuously formed by evolution of dioxygen from lattice oxides, and is continuously quenched upon replenishment by water or hydroxide. We believe that this chemistry may not be restricted to gold and will also occur on other metal oxides during many relevant electrocatalytic reactions. Overall, this work provides a new perspective on how the structure of amorphous oxides changes during a catalytic process, which is seen as one of the most challenging scientific questions for a long time.

3.6 Experimental procedures

Resource availability

Lead contact Further information and requests for resources should be directed to and will be fulfilled by the corresponding author, Dennis G. H. Hetterscheid (d.g.h.hetterscheid@chem.leidenuniv.nl).

Materials availability: This study did not generate new unique reagents.

Data and code availability

All data needed to evaluate the conclusions in the paper are present in the paper or the supplemental information. Full experimental procedures are provided in the supplemental information.

3.7 Acknowledgements

This work was supported from the China Scholarship Council (award number 201706420073).

3.8 References

1. Yuan, C.; Wu, H. B.; Xie, Y.; Lou, X. W., *Angew. Chem. Int. Ed. Engl.* **2014,** *53* (6), 1488-504.
2. Song, J.; Wei, C.; Huang, Z. F.; Liu, C.; Zeng, L.; Wang, X.; Xu, Z. J., *Chem. Soc. Rev.* **2020,** *49* (7), 2196-2214.
3. McCrory, C. C.; Jung, S.; Peters, J. C.; Jaramillo, T. F., *J. Am. Chem. Soc.* **2013,** *135* (45), 16977-87.
4. Hwang, J.; Rao, R. R.; Giordano, L.; Katayama, Y.; Yu, Y.; Shao-Horn, Y., *Science* **2017,** *358* (6364), 751-756.
5. Cheng, X.; Fabbri, E.; Nachtegaal, M.; Castelli, I. E.; El Kazzi, M.; Haumont, R.; Marzari, N.; Schmidt, T. J., *Chem. Mater.* **2015,** *27* (22), 7662-7672.
6. Wang, J.; Gao, Y.; Kong, H.; Kim, J.; Choi, S.; Ciucci, F.; Hao, Y.; Yang, S.; Shao, Z.; Lim, J., *Chem. Soc. Rev.* **2020,** *49* (24), 9154-9196.
7. Ding, H.; Liu, H.; Chu, W.; Wu, C.; Xie, Y., *Chem. Rev.* **2021,** *121* (21), 13174-13212.
8. Yang, S.; Hetterscheid, D. G. H., *ACS Catal.* **2020,** *10* (21), 12582-12589.
9. Gerken, J. B.; McAlpin, J. G.; Chen, J. Y.; Rigsby, M. L.; Casey, W. H.; Britt, R. D.; Stahl, S. S., *J. Am. Chem. Soc.* **2011,** *133* (36), 14431-42.
10. Bergmann, A.; Jones, T. E.; Moreno, E. M.; Teschner, D.; Chernev, P.; Gliech, M.; Reier, T.; Dau, H.; Strasser, P., *Nat. Catal.* **2018,** *1* (9), 711-719.
11. Conway, B. E., *Prog. Surf. Sci.* **1995,** *49* (4), 331-452.
12. Rao, R. R.; Huang, B.; Katayama, Y.; Hwang, J.; Kawaguchi, T.; Lunger, J. R.; Peng, J.; Zhang, Y.; Morinaga, A.; Zhou, H.; You, H.; Shao-Horn, Y., *J. Phys. Chem. C* **2021,** *125* (15), 8195-8207.
13. Beall, C. E.; Fabbri, E.; Schmidt, T. J., *ACS Catal.* **2021,** *11* (5), 3094-3114.
14. Takashima, T.; Hashimoto, K.; Nakamura, R., *J. Am. Chem. Soc.* **2012,** *134* (3), 1519-1527.
15. Subbaraman, R.; Tripkovic, D.; Strmcnik, D.; Chang, K.-C.; Uchimura, M.; Paulikas, A. P.; Stamenkovic, V.; Markovic, N. M., *Science* **2011,** *334* (6060), 1256-1260.
16. Zhang, B.; Zhang, B.; Zhao, G.; Wang, J.; Liu, D.; Chen, Y.; Xia, L.; Gao, M.; Liu, Y.; Sun, W.; Pan, H., *Nat. Commun.* **2022,** *13* (1), 5894.
17. Strmcnik, D.; Kodama, K.; van der Vliet, D.; Greeley, J.; Stamenkovic, V. R.; Marković, N. M., *Nat. Chem.* **2009,** *1* (6), 466-472.
18. Xu, C.; Tian, Z.; Shen, P.; Jiang, S. P., *Electrochim. Acta* **2008,** *53* (5), 2610-2618.
19. Chen, Y.; Li, C. W.; Kanan, M. W., *J. Am. Chem. Soc.* **2012,** *134* (49), 19969-19972.
20. Gu, J.; Héroguel, F.; Luterbacher, J.; Hu, X., *Angew. Chem. Int. Ed.* **2018,** *57* (11), 2943-2947.
21. Laurence D. Burke, L. D. B., Electrochemistry of hydrous oxide films. *Modern Aspects of Electrochemistry* 1986 pp 169-189.
22. Hammer, B.; Norskov, J. K., *Nature* **1995,** *376* (6537), 238-240.
23. Li, C. Y.; Le, J. B.; Wang, Y. H.; Chen, S.; Yang, Z. L.; Li, J. F.; Cheng, J.; Tian, Z. Q., *Nat Mater* **2019,** *18* (7), 697-701.
24. Saavedra, J.; Doan, H. A.; Pursell, C. J.; Grabow, L. C.; Chandler, B. D., *Science* **2014,** *345* (6204), 1599-1602.
25. Peuckert, M.; Coenen, F. P.; Bonzel, H. P., *Surf. Sci.* **1984,** *141* (2-3), 515-532.
26. Weiher, N.; Willneff, E. A.; Figulla-Kroschel, C.; Jansen, M.; Schroeder, S. L. M., *Solid State Commun.* **2003,** *125* (6), 317-322.
27. Burke, L. D.; Nugent, P. F., *Gold Bull.* **1997,** *30* (2), 43-53.
28. Vesztergom, S.; Ujvári, M.; Láng, G. G., *Electrochem. commun.* **2011,** *13* (4), 378-381.
29. Cherevko, S.; Topalov, A. A.; Zeradjanin, A. R.; Katsounaros, I.; Mayrhofer, K. J. J., *RSC Adv.* **2013,** *3* (37).
30. Hubkowska, K.; Łukaszewski, M.; Czerwiński, A., Quartz crystal nanobalance measurements in electrocatalysis. In *Encyclopedia of Interfacial Chemistry*, Wandelt, K., Ed. Elsevier: Oxford, 2018; pp 402-412.
31. Watanabe, M.; Uchida, H.; Ikeda, N., *J. electroanal. chem.* **1995,** *380* (1), 255-260.
32. Daikhin, L.; Gileadi, E.; Tsionsky, V.; Urbakh, M.; Zilberman, G., *Electrochim. Acta* **2000,** *45* (22), 3615-3621.
33. Kautek, W.; Sahre, M.; Soares, D. M., *Ber. Bunsenges. Phys. Chem.* **1995,** *99* (4), 667-676.
34. Wang, L. S., *Phys. Chem. Chem. Phys.* **2010,** *12* (31), 8694-705.
35. Cabrera, N.; Mott, N. F., *Rep. Prog. Phys.* **1948,** *12*, 163-184.
36. Angersteinkozlowska, H.; Conway, B. E.; Tellefsen, K.; Barnett, B., *Electrochim. Acta* **1989,** *34* (8), 1045-1056.
37. Grimaud, A.; Diaz-Morales, O.; Han, B.; Hong, W. T.; Lee, Y. L.; Giordano, L.; Stoerzinger, K. A.; Koper, M. T. M.; Shao-Horn, Y., *Nat. Chem.* **2017,** *9* (5), 457-465.